Article:
MacInnes, J.M. and Ayash, A.A. (2018) Mass transfer characteristics of rotating spiral gas-liquid contacting. Chemical Engineering Science, 175. pp. 320-334. ISSN: 0009-2509

https://doi.org/10.1016/j.ces.2017.10.005

Mass Transfer Characteristics of a Rotating Spiral Gas-Liquid Contactor

J. M. MacInnes* and A. A. Ayash
Chemical and Biological Engineering
University of Sheffield
Mappin Street, Sheffield, S1 3JD, UK
June 2017
*Corresponding author
Tel. +44 (0) 114 222 7511
Email. j.m.macinnes@sheffield.ac.uk

Abstract
The first substantial experimental measurements of mass transfer in a rotating spiral channel are reported for counter-current physical desorption of a range of organic solutes from water into air. General relations in terms of bulk properties are developed that allow analysis and comparison across different solute properties, operating conditions and contacting equipment. The phase flow rate ratio and cleaned-phase throughput per passage volume emerge as parameters of principal importance, the former measuring sufficiency of solvent phase flow and the later mass transfer effectiveness and, consequently, required device size. The analytical solution for an infinitely wide channel is used to probe the finite-width experimental results and an apparently universal pattern of differences involving a peak in mass transfer coefficient emerges. As liquid flow rate decreases, the thickness of the liquid layer decreases and the mass transfer coefficient rises. But with further decrease in liquid flow rate and liquid layer thickness, an increasing fraction of the liquid flows in the corner regions under the end-wall menisci and the poor contact in these regions leads to a falling mass transfer coefficient. The peak is found to occur at a similar liquid layer thickness regardless of gas flow rate or solute equilibrium characteristics. Comparison is made with packed columns and rotating packed beds using available data in the literature. The rotating spiral performance suggests device sizes will be many times smaller than those for the two packed devices considered. Dependence of rotating spiral device volume on the square of channel size is demonstrated, showing that further reduction in device volume is possible.

Key words: rotating spiral channel, mass transfer, desorption, gas-liquid interface, Coriolis acceleration, centrifugal acceleration

1. Introduction

The idea of a rotating spiral channel to guide two fluid phases in counter-current flow was put forward in a series of patents by Podbielniak in the 1930s (Podbielniak, 1935, 1936, 1937, 1938). However, no experimental results from such devices were reported in the literature until the idea was picked up independently by MacInnes et al. (2010, 2012). Podbielniak and his collaborators continued with rotating designs packed with various configurations of concentric cylindrical shells, apparently finding the spiral idea unworkable. In MacInnes and Zambri (2015), this early work was briefly reviewed and it was pointed out that the spiral would have been unsuccessful there for several reasons: the rotation axis was placed horizontally rather than vertically, interface stability limits were likely exceeded and the inlet and outlet configurations at the spiral ends allowed uncontrolled phase interaction.

MacInnes and Zambri (2015) demonstrated successful operation for gas-liquid contacting over a wide range of phase flow rates and liquid layer thickness in a general-purpose research device designed using the analytical theory for an infinite width channel (MacInnes et al., 2012). Detailed determination of interface shape and liquid layer thickness using imaging through a glass cover window and a model for the interface shape showed good agreement with the infinite channel theory, provided the height of the menisci formed at the side walls remained sufficiently small compared to the liquid layer thickness. Most importantly the work showed that the parallel flow of the gas and liquid in approximately uniform layers could be controlled and remain stable over wide ranges of conditions as predicted by the theory. This opens the way now for using the spiral to produce controlled mass transfer at far smaller scale than achieved with any other contacting method. Since the size of a contacting device, for a given throughput, depends on the square of the contacting scale (MacInnes et al., 2012) there is considerable benefit to be gained.

The objective here is to produce a range of mass transfer data and use this to characterise the mass transfer coefficient behaviour and to compare with other types of contactor. In particular, desorption of a dilute organic solute species (ethanol, acetonitrile, acetone or butanone) from water into air using the rotating spiral apparatus of MacInnes and Zambri (2015) are measured over a range of phase flow rates. The most important property of these phase and solute systems is the equilibrium distribution of the solute between the two phases, represented here by the equilibrium ratio of the mole fractions in the solvent phase

(air) and the cleaned phase (water) and given the symbol f_S' (the slope of the equilibrium function). The parameter f_S' may in practice range over orders of magnitude and, since this is linked to the required relative amounts of solvent and cleaned phase that must be used, the flow rate ratio of the two phases also varies considerably and will affect mass transfer performance. Other parameters include the gas and liquid phase Reynolds numbers and ratios of the physical properties of the two phases. The use of the water-air system throughout the present work means that there is relatively little variation in the phase properties and so, for example, the ratio of the phase Reynolds numbers depends approximately only on the flow rate ratio of the phases. Liquid viscosity may in other cases be far greater than that of the water considered here. In previous work using amine solutions to absorb CO_2 from a gas stream (MacInnes et al., 2017) the spiral has been successfully operated with liquid viscosities up to 10 cP and in MacInnes and Zambri (2015) viscosities up to 60 cP were routinely tested. The effect of viscosity on mass transfer is not determined here, but it is clear that the same methods and principles would apply.

A general theoretical framework for physical mass transfer is developed allowing consistent analysis of experimental data for both counter-current and co-current flow, whether for absorption or desorption and whether linear or radial flow is involved. The standard theory (e.g. Sherwood et al. 1975) is presented in a unified form allowing essential features to stand out clearly. Following Edmister (1957), the usual formula for determining overall volumetric mass transfer coefficient is recast as a design equation linking purification with the phase flow rate ratio, the residence time of the cleaned phase and the specific throughput, a contacting effectiveness parameter (MacInnes et al., 2012). The specific throughput is the cleaned phase flow rate per contacting passage volume for one equilibrium stage. Comparison of different devices or conditions, it is argued, should be based on the specific throughput divided by the number of stages required to reach a given purification, which is the throughput per total passage volume. This 'total' specific throughput is the metric used to place the rotating spiral results obtained here into context with alternative devices performing similar separation tasks. Comparison is made with mass transfer data from the literature for packed columns and rotating packed beds, the two most prominent devices in use for achieving continuous counter-current contacting. The distillation data of MacInnes et al. (2010) using a channel that is one fifth the size of the spiral channel used here can also be included to demonstrate the increasing performance with decreasing channel size.

Use of the analytical theory for an infinitely wide spiral channel (MacInnes et al., 2012) will be helpful for interpreting the experimental results from the finite-width experimental channel. In the experimental channel, the liquid layer will have an aspect ratio of at least 20 and the gas layer of about 2.6. These relatively large aspect ratios suggest that the behaviour of an infinite width channel should be relevant if not quantitatively precise. This 'wide channel' model has been used to predict hydrodynamic features in MacInnes and Zambri (2015).

2. Mass transfer relations

Fig. 1 represents the general situation of counter-current flow where the phase that is being cleaned of a solute species flows in the positive x direction and the solvent phase receiving the solute flows in the negative x direction. The total contacting length is L and other key parameters are the phase interfacial area per unit passage volume, a_P, and the volume fraction of the cleaned phase, ξ_C, in the space of the contacting passage. For the desorption experiments conducted here, the liquid phase initially contains the solute species and is thus the cleaned phase and the gas phase into which the solute is desorbed is the solvent phase. But the relations developed in this section apply equally to absorption simply by noting that the cleaned phase is then the gas with the solvent phase the liquid. No significance is attached to the depiction in Fig. 1 of the cleaned phase as a dispersed phase. It could equally be the continuous phase and the dispersed phase could be either drops or bubbles, as the case may be, or indeed neither as is the case for the rotating spiral where the phases do not mix.

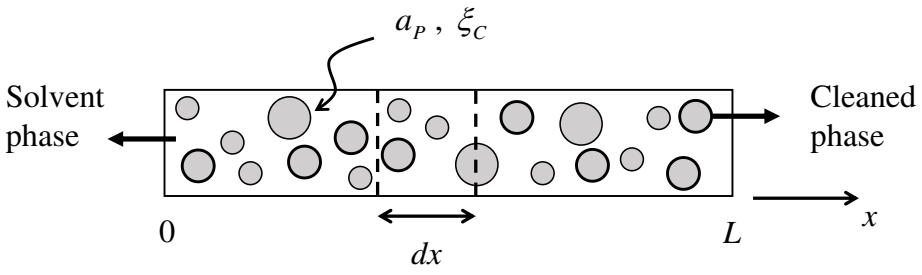

Figure 1. Counter-current fluid-phase contacting nomenclature.

Using the specific interface area based on passage volume, a_P, is a departure from the convention in packed column analysis, where area per volume including that occupied by the packing material (a) is used. Where comparisons are required, the relation $a = \varepsilon a_P$ must be used to place quantities involving specific area on a common basis (ε is the void fraction of the packed column). Interface area per passage volume will be used here since the fraction of solid material involved brings in differences between technologies that may well be open to improvement and therefore would cloud comparisons.

2.1. Dilute solute approximation

Ordinary differential equations in x for the bulk mole fraction of solute in each phase govern the mass transfer. These are subject to continuity of flux and solute equilibrium at the phase interface and the imposed bulk mole fraction values at the inlets. Solution requires numerical computation in general where flow rates, mass transfer coefficients or physical properties may vary with x. When the solute is present in dilute concentrations neither flow rates nor physical properties are altered significantly by species transfer and, for constant mass transfer coefficients, an analytical solution is possible. For the rotating spiral and packed column, constant mass transfer coefficients along the contacting direction is a reasonable approximation. In rotating packed beds, however, average velocity, centrifugal acceleration and, consequently, the mass transfer coefficients, vary in the contacting (radial) direction. Rotating packed bed analysis is taken up at the end of the section.

Also for a dilute solute, the phase equilibrium curve has constant slope (f_S') so

$$Y_S = f_S' \, Y_C \tag{1}$$

(Subscripts 'C' and 'S' are used throughout to designate a cleaned or solvent phase property, respectively.) A single overall mass transfer coefficient (K_C) in terms of those for the individual cleaned and solvent phases (k_C and k_S) can be used:

$$K_C = \left(\frac{1}{f_S' \, k_S} + \frac{1}{k_C} \right)^{-1} \tag{2}$$

The resulting differential equation for bulk solute mole fraction in the cleaned phase is

$$n_C u_{CB} \xi_C \frac{dY_{CB}}{dx} = K_C a_P \left(Y_{CB}^* - Y_{CB} \right) \tag{3}$$

This represents the balance between convection of solute along x and transfer to the solvent phase. Subscript 'B' designates a bulk property and the group $n_C u_{CB} \xi_C$ is molar flow rate of the cleaned phase per unit passage section area in terms of cleaned phase molar density (n_C), cleaned phase average velocity (u_{CB}) and fraction of the passage section (ξ_C) occupied by the cleaned phase. On the right hand side, $Y_{CB}^* = Y_{SB} / f_S'$ is the adjusted bulk solvent phase solute mole fraction, which serves to remove the mole fraction jump at the phase interface and thereby eliminates direct appearance of interface mole fractions.

The bulk mole fraction in the solvent phase at any position x is determined from that in the cleaned phase using overall solute balance:

$$Y_{SB}(x) = Y_{SB}(0) - \frac{Y_{CB}(x) - Y_{CB}(0)}{q_S} \tag{4}$$

where q_S is the ratio of the molar flow rates of the two phases:

$$q_S = \frac{n_S u_{SB}(1-\xi_C)}{n_C u_{CB} \xi_C} \tag{5}$$

Taking the flow rates and the overall volumetric mass transfer coefficient, $K_C a_P$, as constant, Eq. 3 can be integrated (e.g. Sherwood et al., 1975) from $x = 0$ to L to give

$$\frac{K_C a_P L}{n_C u_{CB} \xi_C} = \frac{Y_{CB}(L) - Y_{CB}(0)}{\overline{\Delta Y_{CB}}} \tag{6}$$

$$\text{where} \quad \overline{\Delta Y_{CB}} = \frac{\Delta Y_{CB}(L) - \Delta Y_{CB}(0)}{\ln\left[\Delta Y_{CB}(L) / \Delta Y_{CB}(0)\right]} \quad \text{with} \quad \Delta Y_{CB} = Y_{CB}^* - Y_{CB}$$

Eq. 6 is the usual relation used to determine the overall volumetric mass transfer coefficient from measurements of flow rates and bulk solute mole fractions in the inlet and outlet streams of each phase. Since the specific interface area (a_P) is generally unknown, usually K_C cannot be reliably determined experimentally. Neither can individual volumetric mass transfer coefficients, unless one of them clearly dominates the mass transfer resistance. For the rotating spiral, however, $a_P = 1/h$ (where h is channel height) is an excellent approximation for the experimental conditions used here.

It will be helpful to recast Eq. 6 in terms of the solute mole fractions at the cleaned phase outlet and the solvent phase inlet normalised by the cleaned phase inlet mole fraction:

$$c_C = Y_{CB}(L) / Y_{CB}(0) \qquad c_S = Y_{SB}(L) / Y_{CB}(0) \tag{7}$$

c_C then quantifies the degree of purification achieved (e.g. $c_C = 0$ is complete removal of the solute and $c_C = 1$ is no solute removed) and c_S quantifies the purity of the entering solvent (normally solute is absent from the entering solvent and $c_S = 0$). Eq. 6 can be expressed equivalently in terms of these mole fraction parameters, using Eq. 4 with $x = L$:

$$\frac{K_C a_P L(1 + f'_S q_S)}{n_C u_{CB} \xi_C f'_S q_S} = \ln\left\{\frac{-q_S c_S + f'_S q_S c_C}{1 - c_C - q_S c_S + f'_S q_S}\right\} \tag{8}$$

2.2. Mass transfer effectiveness

Two essential factors affect the mass transfer: the ratio of the phase flow rates and the effectiveness of the phase contacting. The requirement of a sufficient solvent flow rate to carry away all of the solute contained in the entering cleaned phase is straightforward, while the contacting effectiveness is dependent on the complexities of the two-phase flow produced in each particular device. It is important to have a precise measure of this effectiveness so equipment can be compared and improved.

If there is insufficient flow of solvent relative to that of the cleaned phase only a fraction of the solute in the entering cleaned phase can be removed. The critical solvent molar flow rate, for which the cleaned phase exits in equilibrium with the entering solvent phase, may be expressed relative to the cleaned phase molar flow rate using Eq. 4 evaluated at $x = L$ and with $Y_{SB}(0) = f'_S Y_{CB}(0)$:

$$-q_S = \frac{1 - c_C}{f'_S - c_S} \tag{9}$$

The negative sign in front of q_S arises since the cleaned phase flow rate is positive but the solvent phase flow rate is negative for counter-current flow. For pure solvent, Eq. 9 reduces to the important constraint on the phase flow rate ratio,

$$-f'_S q_S > 1 - c_C \tag{10}$$

The parameter on the left hand side is referred to as the stripping factor in desorption work and absorption factor in absorption work (e.g. Edmister, 1957). The factor $-f'_S q_S$ has precisely the same role in the equations regardless of the direction of transfer and here the general term ‘normalised flow rate ratio’ is used, ‘normalised’ referring to the factor of f'_S. Eq. 10 shows directly that removal of a solute with a large value of f'_S will require a

relatively small flow of solvent, while one with a small value of f_S' will require relatively large solvent flow. Violating the inequality simply means there is insufficient flow of solvent to remove the solute from the cleaned phase to the required value of c_C, and the best that can be achieved with counter-current flow is in that case

$$c_C = 1 + f_S' q_S \qquad (0 < -f_S' q_S < 1) \qquad (11)$$

For example, if $-f_S' q_S = 0.7$ the lowest c_C can reach is 0.3.

The second factor affecting mass transfer is the contacting effectiveness and a measure that quantifies this is needed. MacInnes et al. (2012) use the volume flow rate of the cleaned phase per passage volume required for one equilibrium stage, referred to as the specific throughput, Φ_C. In terms of the equilibrium stage length, ℓ_e, specific throughput is then given by

$$\Phi_C = \frac{u_{CB}\xi_C}{\ell_e} \qquad (12)$$

The larger the specific throughput at a given value of $-f_S' q_S$ the smaller the passage volume, and hence device volume, needed to purify a given cleaned phase throughput. The relation for the equilibrium stage length is derived directly from Eq. 6 by taking $x = 0$ to represent an arbitrary position along the contacting and replacing L by ℓ_e. By definition of equilibrium stage length, $Y_S(0) = f_S' Y_C(\ell_e)$; using this and overall mole balance (Eq. 4 with $x = \ell_e$),

$$\ell_e = \frac{n_C u_{CB}\xi_C}{K_C a_P} \frac{f_S' q_S \ln(-f_S' q_S)}{(1 + f_S' q_S)} \qquad (13)$$

and substitution into Eq. 12 gives the relation for specific throughput:

$$\Phi_C = \frac{K_C a_P}{n_C} \frac{(1 + f_S' q_S)}{f_S' q_S \ln(-f_S' q_S)} \qquad (14)$$

Since Φ_C is throughput per equilibrium stage volume, it does not represent throughput per device size, which depends also on the number of stages required. The number of stages is given by $N = L/\ell_e$, which can be seen to differ from Φ_C precisely by a factor of mean residence time of the cleaned phase:

$$t_{mC} = \frac{L}{u_{CB}\xi_C} \qquad (15)$$

Thus, the product of Eqs. 14 and 15, using Eq. 8 to express the mass transfer coefficient, gives a relation for N in terms of purity parameters c_C and c_S:

$$N = \Phi_C t_{mC} = -\frac{1}{\ln\left(-f_S' q_S\right)} \ln\left\{\frac{-q_S c_S + f_S' q_S c_C}{1 - c_C - q_S c_S + f_S' q_S}\right\} \qquad (16)$$

This shows clearly that the number of stages required to achieve a given purity depends on the choice of the flow rate ratio. As $-f_S' q_S$ increases, Eq. 14 gives a decreasing Φ_C but Eq. 16 gives a decreasing number of stages to achieve a given purification (c_C). In order to compare performance at different flow rate ratios ($-f_S' q_S$) it is therefore necessary to specify the purification to be reached (as well as the solvent purity, c_S) and look at the throughput per total passage volume, given by:

$$\Phi_{CN} = \frac{\Phi_C}{N} = \frac{K_C a_P}{n_C} \frac{\left(1 + f_S' q_S\right)}{f_S' q_S} \left[\ln\left\{\frac{-q_S c_S + f_S' q_S c_C}{1 - c_C - q_S c_S + f_S' q_S}\right\}\right]^{-1} \qquad (17)$$

It is helpful to plot this function to make clear the effect of $-f_S' q_S$ on this 'total' specific throughput. For constant $K_C a_P / n_C$, $c_S = 0$ and normalising Φ_{CN} by $\Phi_{CN\infty}$ (the limit as $-f_S' q_S \to \infty$), Fig. 2 shows (solid curves) the change with $-f_S' q_S$ for the three purification values, c_C = 0.1, 0.01 and 0.001. For reference, the individual changes in Φ_C and N with $-f_S' q_S$ are also plotted. As the normalised flow rate ratio is decreased towards $1 - c_C$ (Eq. 10) the total specific throughput is increasingly attenuated by the rapidly increasing number of stages to reach the specified purification, with only slight moderation from the increasing Φ_C level.

On the other hand, high flow rate ratios require excessive solvent flow rate. The precise optimum for $-f_S' q_S$, for a given phase and solvent system, will depend on the values of the purity parameters, on how $K_C a_P / n_C$ changes with $-f_S' q_S$ and on economic factors external to the contacting operation itself and must be determined for each situation individually. However, a value in the range $-f_S' q_S = 2$ to 6 would seem reasonable for the trade-off between device size (total specific throughput) and solvent cost (flow rate ratio). For example, c_C = 0.1 allows 70 to 90% of the maximum possible total specific throughput to be reached in that range of solvent flow rate.

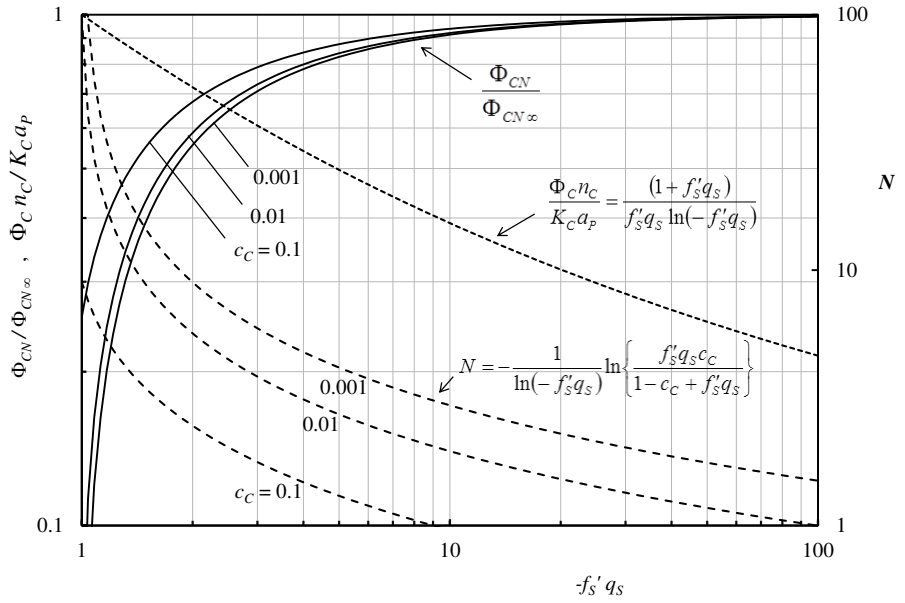

Figure 2. Trade-off between specific throughput and solvent flow rate for three different purification values.

2.3. Purification formula

Eq. 16 relates parameters of primary physical significance in a single relation. Rearranging this to express explicitly the purification, c_C, as a function of specific throughput, mean residence time, solvent inlet purity and normalised flow rate ratio gives (Edmister, 1957):

$$c_C = \frac{q_S c_S + (1 - q_S c_S + f_S' q_S)(-f_S' q_S)^{-\Phi_C t_{mC}}}{f_S' q_S + (-f_S' q_S)^{-\Phi_C t_{mC}}} \qquad (18)$$

The number of stages has been expressed in terms of specific throughput and residence time, i.e. as $\Phi_C t_{mC}$, so the effect of improved contacting (Φ_C) can be distinguished from merely increasing residence time (t_{mC}). Only increasing the specific throughput reduces device size; increasing the residence time at fixed Φ_C to improve purification always increases device size. At a given value of $-f_S' q_S$, increasing $\Phi_C t_{mC}$ improves the purification, independent of whether this is the result of larger residence time or larger specific throughput. The flow rate ratio produces a rapid rise in c_C as $-f_S' q_S$ falls below the minimum value satisfying Eq. 10, i.e. when there is insufficient solvent flow rate to remove all of the entering solute.

(These characteristics are shown later in Fig. 6 where Eq. 18 is plotted with experimental data.)

2.4. Co-current flow

It is worth noting that with co-current flow it is still possible, with sufficient solvent flow, to purify a solute-carrying stream. Eq. 6 applies equally to co- and counter-current flow, but with co-current flow the solvent inlet is now at $x = 0$ rather than at $x = L$ (Fig. 1), the flow rate ratio is positive and the normalised mole fraction of the entering solvent phase is

$$c_S = Y_{SB}(0)/Y_{CB}(0) \tag{19}$$

Using this definition in Eq. 6 leads to the co-current flow relation for c_C,

$$c_C = \frac{1 + f_S' q_S e^{-\zeta} + q_S c_S \left(1 - e^{-\zeta}\right)}{1 + f_S' q_S} \tag{20}$$

ζ is just the left hand side of Eq. 8 and, as there, represents the effectiveness of the contacting. The lowest c_C can be at a given value of $f_S' q_S$ is given by the limit as $\zeta \to \infty$, which from Eq. 20 is $c_C = 1/\left(1 + f_S' q_S\right)$ for a solute-free inlet solvent stream. This limit corresponds to the two phases exiting the contacting at equilibrium.

2.5. Rotating packed beds

In the case of a rotating packed bed, the geometry is cylindrical with flow in the radial direction through a bed with axial height H extending from an inner radius r_I to an outer radius r_O. The formulas given in the preceding sections are in some cases different for this cylindrical geometry since section area varies in the flow direction. The average radial velocity varies with radial position as does the tangential component, which is non-zero due to the rotating packing. These variations can be expected to produce associated variations in the volumetric mass transfer coefficients and analytical solution is not possible. The usual practice is to treat the mass transfer coefficient as constant and consider the resulting formula to involve an effective mass transfer coefficient. Since the average velocity and section area vary, it is convenient to express the flow in terms of the constant volume flow rate of the cleaned phase, $Q_C = u_{CB} \xi_C A$, where $A = 2\pi r H$, which gives in place of Eq. 6 (e.g. Chiang et al., 2009):

$$\frac{\overline{K_C a_P}\,\pi H\varepsilon\left(r_O^2 - r_I^2\right)}{n_C Q_C} = \frac{Y_{CB}(r_O) - Y_{CB}(r_I)}{\overline{\Delta Y_{CB}}} \tag{21}$$

So Eq. 8 becomes

$$\frac{\overline{K_C a_P}\,\pi H\varepsilon\left(r_O^2 - r_I^2\right)\left(1 + f_S' q_S\right)}{n_C Q_C f_S' q_S} = \ln\left\{\frac{-q_S c_S + f_S' q_S c_C}{1 - c_C - q_S c_S + f_S' q_S}\right\} \tag{22}$$

The volumetric mass transfer coefficient, $\overline{K_C a_P}$, appearing in these two equations is the effective one defined as

$$\overline{K_C a_P} = \frac{2}{\varepsilon\left(r_O^2 - r_I^2\right)}\int_{r_I}^{r_O} K_C a_P\, r dr \tag{23}$$

where $K_C a_P$ is the local value that depends on radial position in the bed. The formulas for specific throughput (Eq. 14), number of stages (Eq. 16) and consequently for total specific throughput (Eq. 17) are unchanged, as are those for c_C (Eqs. 18 and 20), provided ζ is taken as the left hand side of Eq. 22 and the mean residence time is defined as

$$t_{mC} = \frac{\pi H\varepsilon\left(r_O^2 - r_I^2\right)}{Q_C} \tag{24}$$

3. Experiment

The apparatus used here is the rotating spiral device described in MacInnes and Zambri (2015) that allows contacting of two immiscible fluid phases in a channel with a rectangular section of height 1.5 mm, width 4.0 mm and length 0.91 m. The spiral makes approximately 5.5 revolutions, with the ends at radial positions of 16.5 mm and 36.7 mm (measured to the outer wall of the channel). The fluids are transferred to and from the rotating unit using pairs of lip seals linked to holes in a rotating shaft on which the spiral is mounted. The spiral channel is milled into a PEEK element, along with holes connecting the spiral ends to those in the shaft, and is closed using a toughened circular glass plate to allow optical access. Heat from both seal and bearing friction is moderated by water flow through additional holes in the shaft, connected using a further two lip seal pairs. Adjusting the cooling water flow rate allows temperature in the spiral channel to be changed.

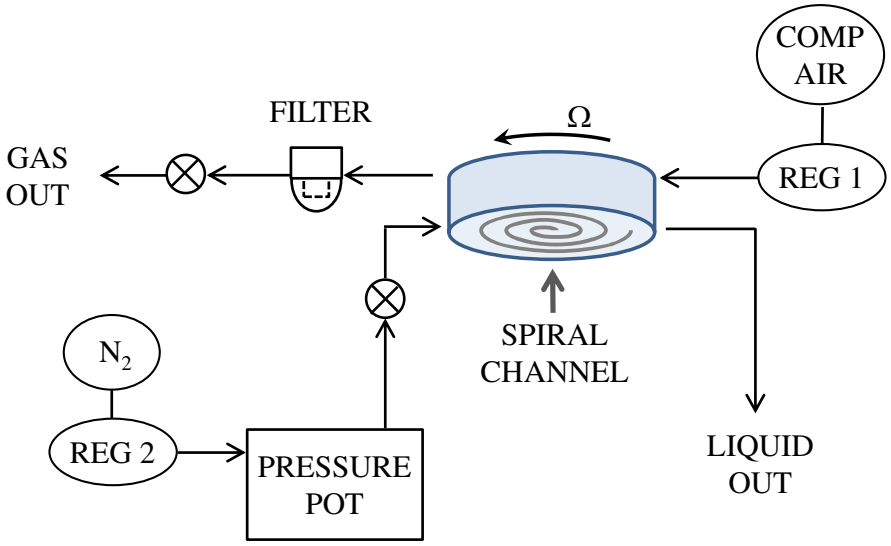

Figure 3. Schematic of the apparatus.

The flow system is as shown in Fig. 3. The liquid is driven from a bottle contained in a pressure pot up through a dip tube leading through a needle valve; gas is supplied from lab compressed air. The liquid exits to atmospheric pressure and this, with the centrifugal hydrostatic change and frictional losses back to the outer end of the spiral channel, determine the liquid pressure there. The gas pressure at this position must match this pressure and is adjusted using REG 1, with the required gas flow rate achieved by adjustment of the downstream gas needle valve. The filter shown in Fig. 3 allows water to condense from the exit gas as it adjusts from the relatively warm spiral temperature to that of the lab. This avoids possible obstruction of the gas needle valve.

In the experiments here, mass transfer characteristics are determined using desorption of organic solute species from dilute solutions with water into air. The four different solute species ethanol, acetonitrile, acetone and butanone are used at three different contacting temperatures (24, 30 and 49 °C), the temperatures in the spiral being set using cooling water flow rate and determined indirectly using the method described in MacInnes and Zambri (2015). Absolute pressure on the spiral is expected to vary along the length by less than 1.5% and this pressure is determined by a hydrostatic calculation working back from the liquid outlet to the outer end of the spiral, as described in the same reference. It is closely the same for all tests, varying only as a result of the minor variation in liquid density due to outlet liquid composition differences. The different temperatures, however, give considerably

different values of f_S' for a given solute in the water-air system and also affect phase properties.

All of the tests are made at a rotation rate of 3200 rpm, for which the liquid layer is known to remain reasonably uniform in thickness with relatively minor meniscal rise. At this rotation rate and for pure water, the model presented in MacInnes and Zambri (2015) (which agreed with measurements of minimum liquid layer thickness and critical refraction position on the interface) produces the interface shape shown in Fig. 4 in the cross-section of the experimental channel. The small amounts of solutes added to the water in the experiments should not greatly change the surface tension and contact angles with the end walls and, hence, the interface shape shown. The figure shows a liquid layer thickness of 120 μm (measured at its minimum). This corresponds to a water flow rate of approximately 13 mL/min, which is at the upper end of the range used in the experiments. Reducing the liquid flow rate simply shifts the shape closer to the outer wall. At the lowest liquid flow rate of about 0.2 mL/min used here, the minimum thickness of the liquid layer is below 20 μm, according to the measurements of MacInnes and Zambri (2015). In that case, the thickness of the liquid layer is of similar thickness to the line used to draw the interface in Fig. 4 leaving the liquid to flow almost entirely in the corner regions under the menisci.

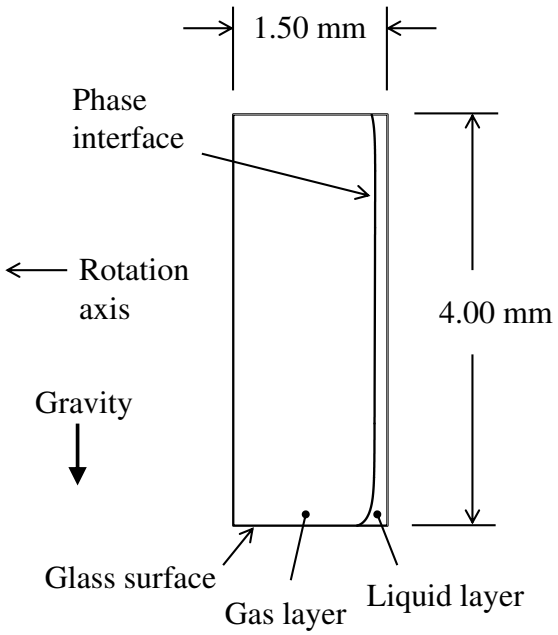

Figure 4. Computed interface shape for air-water contacting at 3200 rpm, represented to scale and for a liquid layer with minimum thickness 120 μm.

3.1. Physical properties

The four different solute species and the three different temperatures are combined to produce seven 'phase and solute systems' giving values of f_S' spanning the range $0.2 < f_S' < 6$. These combinations are listed in Table 1 together with the physical properties needed to characterise the phase and solute properties for both the experimental analysis and the wide-channel model calculations. f_S' values have been determined using the modified Raoult's law with activity coefficients determined using the UNIQUAC model (Anderson and Prausnitz, 1978). The equilibrium curves thus generated are not precisely linear. However, fitting a line to each true curve deviated by typically less than about 3% rms over the range of composition used in the experiments. The table lists for each solute the maximum liquid mole fraction, i.e. that in the liquid feed, $Y_C(0)$. The decreasing liquid inlet mole fraction with increasing f_S' ensures the solute remains dilute in both phases.

Table 1. Physical properties of the seven experimental phase and solute systems.

Solute	T_{spiral} (°C)	f_S'	$Y_C(0)$	ρ_C (kg/m^3)	ρ_S (kg/m^3)	μ_C (10^{-3} Pa s)	μ_S (10^{-5} Pa s)	D_C (10^{-9} m^2/s)	D_S (10^{-6} m^2/s)
Ethanol	30	0.232	0.050	978	2.06	1.19	1.85	1.53	7.11
Ethanol	49	0.651	0.050	966	1.93	0.668	1.94	2.36	7.92
Acetonitrile	30	0.812	0.030	985	2.07	0.843	1.85	1.58	7.79
Acetone	24	1.15	0.020	986	2.11	1.02	1.83	1.15	5.93
Acetonitrile	49	1.84	0.030	976	1.94	0.579	1.94	2.43	8.66
Acetone	49	3.83	0.020	978	1.94	0.632	1.94	2.07	6.67
Butanone	49	5.50	0.015	973	1.94	0.551	1.94	1.77	5.92

Properties of the gas are those for perfect dilution (i.e. for dry air) determined using kinetic theory approximations; density and viscosity are calculated using the ideal gas law and the Sutherland approximation, respectively. Gas phase diffusion coefficients are calculated using the formula in Fuller et al. (1969). The liquid phase properties are determined for the inlet mixture composition. Values of density and viscosity for each liquid inlet composition are taken from experimental data available in the literature (Khattab et al.,

2012; Saleh et al., 2006; Thomas and McAllister, 1957), although density and viscosity in the case of butanone is determined from pure component values using a volume mixing rule. Finally, solute diffusion coefficients are estimated using the Wilke and Chang (1955) correlation with association factor equal to 2.26 (Hayduk and Laudie, 1974).

3.2. Composition measurement

Solute mole fraction in the feed liquid is known from accurate preparation of the solutions and the values are those listed in Table 1. The mole fraction in the entering air stream is zero and so only the outlet solute mole fractions are required to complete the composition information required to calculate $K_C a_P$ values using Eq. 6. In the experiments, the liquid phase outlet composition is measured and outlet gas phase composition is determined from solute mole balance (Eq. 4 with $x = L$). Samples were collected in vials downstream of the liquid outlet from the spiral. When a new flow condition was set in the tests, sufficient time was allowed for the composition in the entire downstream passage to reach steady state, before collecting a sample. This time was determined by extensive tests at different liquid and gas flow rates and for all of the phase and solute systems, in which samples were collected at different times following a large change in gas flow rate to produce an approximate step change in liquid outlet composition. In all cases the steady state mole fraction value at the sampling point was achieved to within a few percent by 12 of the residence times $\tau_C = V_C / Q_C$, where V_C = 1.6 mL is the estimated downstream passage volume. At the lowest flow rates, the time to reach steady state was as long as 2 hours, but more commonly it was less than 10 minutes.

The mole fraction of each collected sample was measured by a calibrated analytical method suited to the particular solute. The uncertainty in each case was less than 1% of the maximum liquid phase mole fraction, although in the case of acetonitrile the uncertainty was somewhat greater at 1.4%. Spectrophotometry was used to determine solute mole fractions in the acetone and butanone samples; gas chromatography was used in the case of ethanol (thermal conductivity detection) and acetonitrile (flame ionisation detection). Blanks of known composition were in all cases analysed together with actual samples as a check on the calibration. Also, liquid feed composition was confirmed by measurement of a sample collected from the supply mixture both at the beginning and at the end of each experimental session.

3.3. Flow rate measurement

The final quantities needed to calculate the mass transfer properties outlined in Section 2 are the phase flow rates. These are measured at the outlets using collection over time. In the case of liquid flow, collected mass is determined by weight to calculate the liquid volume flow rate, knowing liquid density. Gas volume from the outlet is collected in an upturned graduated cylinder immersed in a sink filled with water (giving flow rate at normal pressure and temperature). The flow rates change with distance along the channel due both to solute transfer and to water evaporation, the flow rates of both phases decreasing with increasing x position. The dilute solute concentrations ensure the change in the flow rate associated with solute transfer for either phase remains less than 7%. The effect of water evaporation is also generally small, increasing the gas flow rate by less than 7%, the largest error at the highest operating temperature (49 °C). For the liquid flow rate, however, the relative change at low liquid flow rates could be very large and results with excessive change are excluded from the final data, as described in Section 3.4.

In all cases, the flow rate values were taken as the average of the inlet and outlet values for each phase. The inlet and outlet values were estimated from the measured outlet flow rates using mole balances that assumed the gas to be saturated with water both at the exit from the spiral (at the spiral temperature) and at the collection point (lab temperature). In these mole balances, the liquid mole density was taken as constant and equal to the average of the inlet and outlet values. Two dimensional computations (ANSIS/Fluent Version 16) of the gas flow along the spiral, using a wall boundary condition at a fixed water mole fraction to represent the phase interface, showed that the exiting gas reaches complete saturation for all gas flow rates. Since liquid velocity remains far lower than that of the gas, treating the interface as a fixed surface does not lead to significant approximation. Saturation at the collection point is ensured by long residence time while exposed to ambient lab temperature.

3.4. Measurement uncertainty

The values of either $K_C a_P$ or Φ_C determined from the experiment depend on three principle measured quantities: the liquid flow rate, the gas flow rate and the bulk solute mole

fraction in the exiting liquid. (The gas flow rate is needed so that q_S can be determined to calculate $Y_{SB}(0)$ from Eq. 4.) In addition, the value of liquid mole density (n_C) must be known to calculate $K_C a_P$ from Eq. 6. In reaching that equation, constant flow rates and properties were assumed whereas the solute transfer together with evaporation of the water both cause variation of flow rates and the molar density of the liquid along the channel. The uncertainly associated with flow rate variation can be assessed by recalculating $K_C a_P$ using flow rates at the phase inlets rather than average values for each data point and noting the change. Similarly, uncertainty associated with liquid mole density was assessed by substituting the value for pure water for the average of inlet and outlet mole densities. Finally, the uncertainty associated with solute mole fraction in the outlet liquid stream was determined by noting the change when the measured mole fraction was increased by one standard deviation of the corresponding calibration data from the fitting function. The changes associated with flow rates and with mole fraction measurement were the principal sources of uncertainty and were greatest at low values of liquid flow rate, affecting data at high values of $-f_S' q_S$. All data for which the change associated with any one of the above tests exceeded 12% were excluded from the final data. This figure is considered to be a conservative estimate of the maximum uncertainty in the data presented for mass transfer coefficient and specific throughput.

4. Results

For each of the seven different phase and solute systems in Table 1, the solute mole fraction at the liquid outlet was measured over a range of cleaned phase (liquid) flow rates, Q_C, at each of three different solvent (gas) flow rates: Q_S = 1.3, 3.0 and 6.2 NL/min. Fig. 5 shows plots of the measured normalised values of liquid outlet mole fraction (the purification, c_C) as a function of Q_C for each of the three solvent flowrates, together with analytical solutions at corresponding conditions for an infinitely wide channel (MacInnes et al., 2012). The symbols are experimental points and the model is shown as dashed curves shaded dark to light with increasing solution flow rate.

In all cases, decreasing the cleaned phase flow rate leads to improved purity, i.e. smaller c_C. A lower cleaned phase flow rate relative to the fixed solvent flow rate ensures both adequate solvent supply and purer bulk solvent at any position along the contacting. As

expected, the cleaned phase flow rate producing a given level of purification (c_C) at a given solvent flow rate increases with f_S' since the same amount of solvent can hold more solute as f_S' increases. Similarly, the cleaned phase flow rate at fixed purification increases with the solvent flow rate. These trends are found for both the experiment and the model calculation. However, the model gives a less pronounced change both with solvent flow rate and with f_S', differences that must certainly be caused by the effects of the end walls present in the experimental spiral channel but not in the model that applies to infinite channel width (vertical direction in Fig. 4). The results show that in the experiment the mass transfer is increasingly improved relative to an infinite width channel as f_S' increases. In the infinite width model, the mass transfer coefficients are independent of Reynolds number (MacInnes et al., 2012). Since increasing f_S' corresponds to increasing Q_C for fixed Q_S, both the Reynolds number of the liquid flow and the liquid layer thickness increase with f_S' and these factors clearly can have an effect on the mass transfer. The greater change in the mass transfer with gas flow rate in the experiment also suggests a Reynolds number effect, this time associated with the gas phase Reynolds number.

Plotting the results in terms of the normalised phase flow rate ratio, $-f_S'q_S$, places them into the context of the purification function developed in Section 2.3. Fig. 6 shows all of the data from Fig. 5 plotted in this way along with the purification function (Eq. 18), with $c_S = 0$ as is appropriate and for values of $\Phi_C t_{mC}$ = 0.4, 0.8, 1.6, 3.2, 6.4 and 12.8. The data are plotted as circles with solvent flow rate distinguished by shading: dark to light with increasing Q_S. The data respect as they must the lower limit on c_C imposed by solute mass balance at perfect equilibration ($Y_{SB}(0) = f_S'Y_{CB}(0)$), but fan out over a range of the parameter $\Phi_C t_{mC}$ and hence purification. One might be tempted to judge the success of the contacting for any given test in terms of the value of $\Phi_C t_{mC}$ achieved. However, as mentioned in Section 2.3, improved purification may simply be the result of allowing a longer residence time, t_{mC}, which does not reduce device size unless it is accompanied by an increase in specific throughput, Φ_C. At a given value of q_S, the cleaned phase residence time is inversely related to solvent phase flow rate. Since the results are clearly stratified according to solvent flow rate and hence residence time, the variation in $\Phi_C t_{mC}$ displayed by the data

may be largely the result of variation in the residence time and contacting effectiveness cannot be easily deduced from the plot.

The result for the minimum c_C achievable with co-current flow (Sec. 2.4) is shown as a dashed line on the plot. It is not surprising that the counter-current result for one equilibrium stage, i.e. $\Phi_C t_{mC} = 1$, would precisely overlie the dashed curve if plotted.

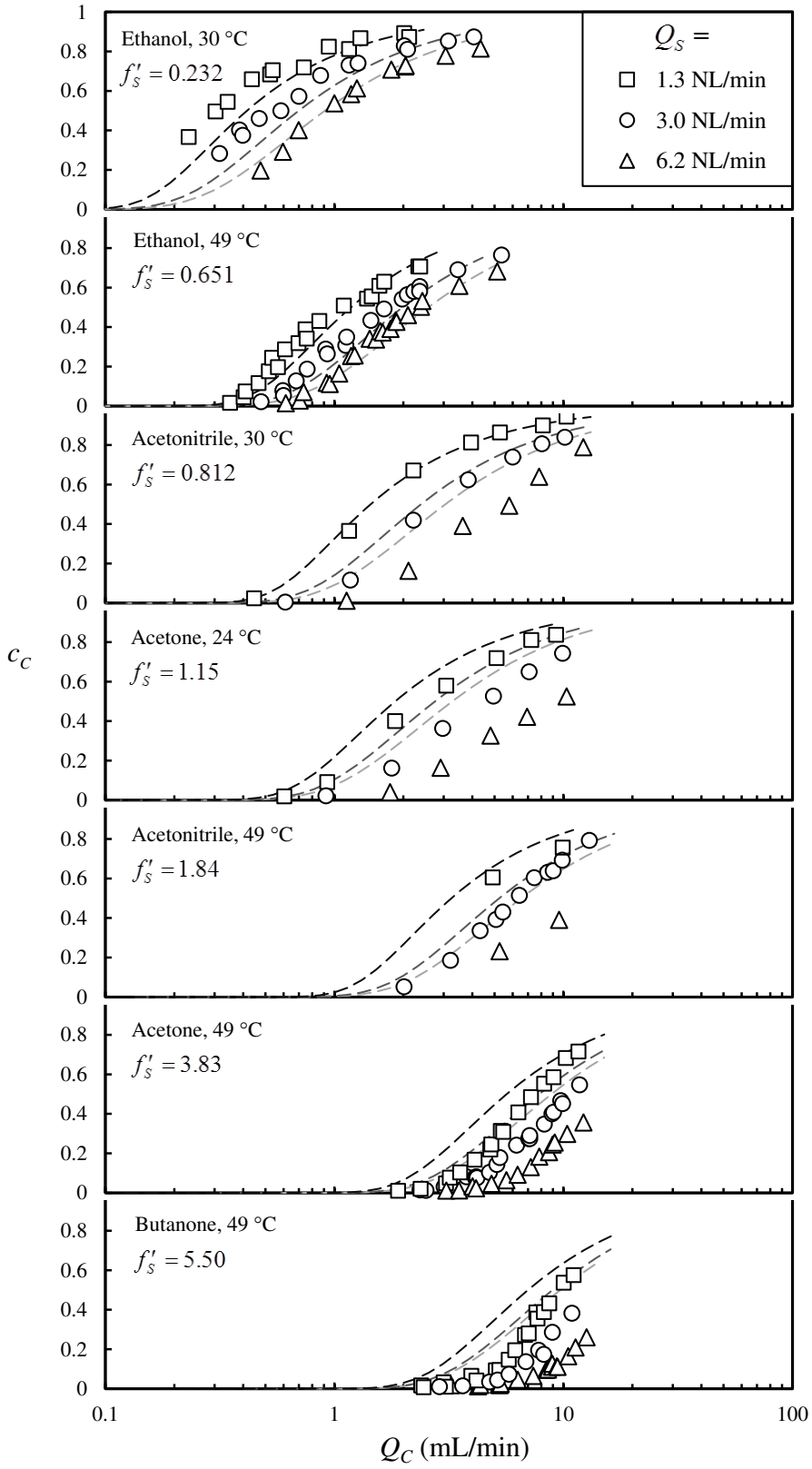

Figure 5. Measured purification (c_C) at the three fixed gas flow rates as liquid flow rate is varied. The dashed lines, shaded dark to light with increasing gas velocity, are calculations using the infinite channel width theory (MacInnes et al., 2012).

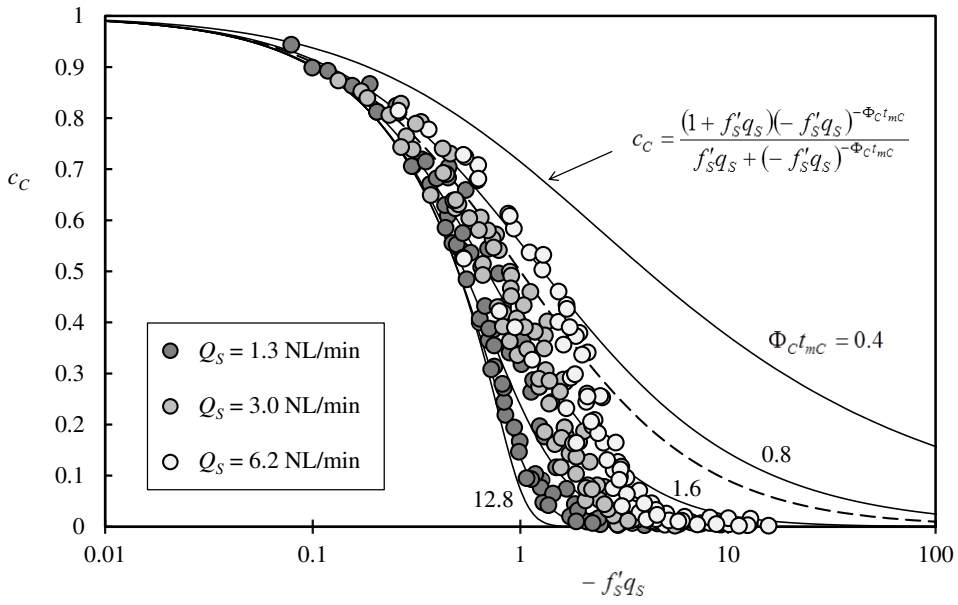

Figure 6. All of the data (symbols) plotted in terms of normalised flow rate. Curves are the purification relation (Eq. 18 with $c_S = 0$). (The dashed line shows the co-current flow result for infinite contacting effectiveness, Eq. 20 for $\zeta \to \infty$, where the abscissa is absolute value of $f_S'q_S$.)

4.1. Mass transfer coefficients

To judge contacting effectiveness, one must look at the specific throughput, Φ_C, on its own. From Eq. 14, Φ_C is equal to the product of $K_C a_P / n_C$ and a function of $-f_S'q_S$. Thus, at a particular value of $-f_S'q_S$ it is helpful first to examine $K_C a_P$ behaviour to understand that of Φ_C. Fig. 7 shows the overall volumetric mass transfer coefficient results at three representative f_S' values plotted as a function of normalised flow rate ratio, $-f_S'q_S$. The circles, diamonds and triangles indicate results for acetone at 49 °C ($f_S' = 3.83$), acetonitrile at 30 °C ($f_S' = 0.812$) and ethanol at 30 °C ($f_S' = 0.232$), respectively, with shading indicating solvent flow rate as before (dark to light as Q_S increases). The corresponding results for infinite channel width are also plotted for comparison (dashed curves, also dark to light as Q_S increases). Again one sees the more pronounced sensitivity of the experimental results to both f_S' and Q_S in relation to the model, but before pursuing the causes of these differences the common trends are examined.

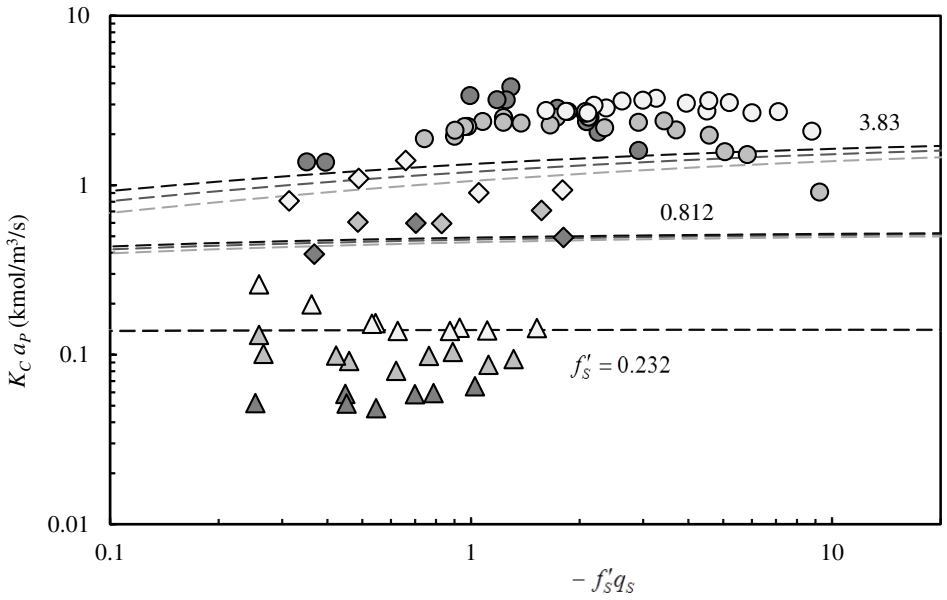

Figure 7. Overall volumetric mass transfer coefficient for $f_S' = 0.232$, 0.812 and 3.83. Symbols are experiment for $Q_S = 1.3$, 3.0 and 6.2 NL/min (shaded dark to light with increasing gas flow rate). The dashed curves are the infinite channel results for the same f_S' and Q_S values as the experiment (again, shaded dark to light with increasing gas flow rate).

Perhaps the principal observation from Fig. 7 is that $K_C a_P$ increases with f_S'. Since $a_P \approx 1/h$ is not changing, K_C must be. Increasing f_S' will clearly increase the gas phase contribution ($f_S' k_S$ in Eq. 2) to K_C, provided k_S does not decrease strongly. At fixed Q_S a roughly constant value of gas phase mass transfer coefficient is expected. The multiplication of k_S by f_S' in Eq. 2 is a direct consequence of using Y_C^* as the gas mole fraction variable, which in addition to removing the interface jump in mole fraction also decreases the gas phase mole fraction gradient in terms of that variable as f_S' increases, since $dY_C^*/dy = (dY_S/dy)/f_S'$. Thus, K_C must increase with increasing f_S' at fixed $-f_S' q_S$ and Q_S simply as a result of the adjusted gas phase mole fraction variable in the bulk mole fraction difference, $Y_{CB}^* - Y_{CB}$, used to define it. A plot of Φ_C would look the same as that for $K_C a_P$ (Fig. 7) except that the data and curves would be uniformly tilted by the factor of flow rate ratio in Eq. 14, which is a decreasing function of $-f_S' q_S$ (Fig. 2). Thus, Φ_C also increases with f_S' at fixed $-f_S' q_S$ and Q_S.

But the increase in $K_C a_P$ with f_S' is strong only if the solvent phase mass transfer coefficient makes a significant contribution. The individual mass transfer coefficients can be calculated for the wide channel model results and these are shown in Fig. 8 as functions of f_S' for the intermediate gas flow rate Q_S = 3.0 NL/min, the condition $-f_S' q_S = 1$ and with averages of the values listed in Table 1 used for each phase property in the calculation. The individual mass transfer coefficients show a roughly uniform gas phase value, as expected, and a decreasing liquid phase value as f_S' increases, also as expected. The increasing value of $f_S' k_S$ with f_S' that results, however, remains lower than k_C up to about $f_S' = 4$, so the liquid phase mass transfer has a relatively minor though increasing influence up to this value of f_S' . Beyond $f_S' = 4$ the liquid phase mass transfer coefficient continues to increase but does not fully dominate the overall coefficient until well beyond the range of the experiments. This conclusion is not substantially changed for the other gas flow rates or for other values of $-f_S' q_S$. k_S and, hence, $f_S' k_S$ is not affected and k_C is somewhat increased as $-f_S' q_S$ increases and Q_S decreases (both reducing liquid layer thickness).

The solid diamond symbols in Fig. 8 are the experimental results interpolated to $-f_S' q_S = 1$. These show the same pattern of difference from the wide channel calculations as in Fig. 7. Mass transfer is less effective than in the model at low values of f_S', but more effective at high values. K_C has been determined from the experimental values of $K_C a_P$ using the interface length per volume determined for the calculated shape shown in Fig. 4, which is $a_C = 1.015/h$.

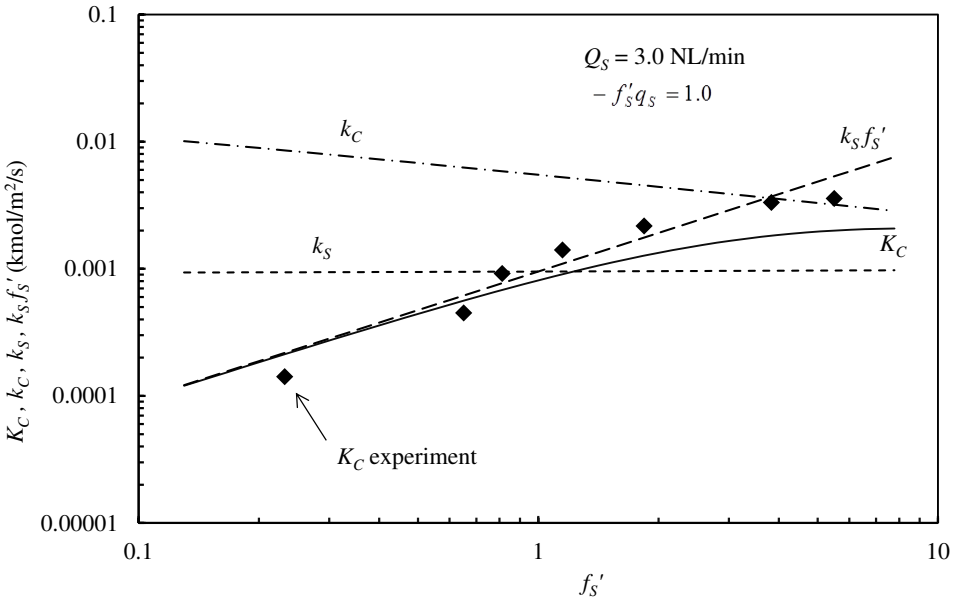

Figure 8. Dependence for infinite channel width of the components of overall mass transfer coefficient on f_S' for $-f_S' q_S = 1$ and Q_S = 3.0 NL/m. Symbols are values interpolated from the experimental results and using $a_C = 1.015/h$.

Turning to the quantitative differences between the finite channel experimental results and the infinite channel predictions in Fig. 7, the greater change in the overall mass transfer coefficient with both f_S' and Q_S must be a consequence of the end walls, i.e. the top and bottom boundaries in Fig. 4. These interrupt the phase layers and phase interface producing two identifiable changes relative to an infinite width channel (MacInnes and Zambri, 2015). First, the phase interface is distorted from a surface parallel to the side walls by the contact angle enforced at the end wall surfaces. Fig. 4 shows this effect together with the slight tilt of the layer due to gravity. So it is clear that as the liquid flow rate decreases, and hence also the liquid layer thickness decreases, the central part of the layer will become progressively thinner in relation to the corner flow regions beneath the menisci, with an increasingly large fraction of the overall flow in those corners. The second consequence is the generation by Coriolis acceleration of secondary motions adjacent to the end walls in each phase layer (Ortiz-Osorio et al., 2009). The Coriolis motion is dependent on the lateral variations in streamwise velocity and these are large in the vicinity of the end walls where the velocity in both phases is reduced by the 'no slip' requirement. Thus, Coriolis motions are expected to be significant throughout the entire section of gas flow, since it occupies a section of relatively small aspect ratio, but in just the corner regions of the liquid layer. Further, it is

noted that the Reynolds number of the gas flow is far higher than that typical of the liquid flow in the experiments, so Coriolis convection is likely to be stronger in the gas phase.

With these end-wall effects in mind, some of the deviations in Fig. 7 can begin to be understood. It is helpful to consider the results for $f_S' = 3.83$. For each of the three gas flow rates in that case, there is a common pattern: the mass transfer coefficient first increases, reaches a peak and then decreases as $-f_S' q_S$ increases. As $-f_S' q_S$ increases at fixed Q_S, the liquid flow rate is decreasing and as a consequence the liquid layer thickness is also decreasing. It seems likely, given the effects of the end walls outlined above, that the changing liquid layer thickness may help to explain the existence of the observed peak. The liquid layer thickness is considerably smaller over the wide central region of the liquid layer than in the corners under the menisci. In the experiments, the central region ranges in thickness from around 20 to 120 μm while the meniscus on the glass side rises to a height of about 180 μm (MacInnes and Zambri, 2015). So it seems clear that the mass transfer effectiveness, which is dependent on the inverse of thickness, will be significantly larger in the central region than in the corners even though the later are helped by Coriolis convection. Thus, as $-f_S' q_S$ increases, the liquid phase mass transfer coefficient rises as a result of the decreasing liquid layer thickness, but with continued increase in $-f_S' q_S$ the thinning central layer passes a decreasing fraction of the liquid flow and eventually the liquid phase mass transfer coefficient falls as it is increasingly dominated by the poor mass transfer in the corner regions.

The position of the peak, again for $f_S' = 3.83$, shifts to higher $-f_S' q_S$ as Q_S increases. This supports the idea that a particular value of liquid layer thickness determines the peak. At higher Q_S and since the gas flow rate does not greatly affect liquid layer thickness (MacInnes and Zambri, 2015), the liquid flow rate must be the same at the peak regardless of the gas flow rate. But this corresponds to the peak moving to larger $-f_S' q_S$ as Q_S increases, as observed. While the same rise and fall in mass transfer coefficient is not clear in the case of the other two f_S' values shown in Fig. 7, these may simply not span the required range of $-f_S' q_S$. Just as Q_S shifts the peak, decreasing f_S' at fixed Q_S corresponds to a lower $-f_S' q_S$ at the liquid phase flow rate of the peak.

The above argument assumes that the individual liquid phase mass transfer coefficient has a significant effect on the overall coefficient. This was the case for the relatively large

value of f_S' considered above, at least at $-f_S'q_S = 1$ according the wide channel results shown in Fig. 8. A similar plot can be made over the range of $-f_S'q_S$ that covers the experiments and this is shown in Fig. 9 for the three particular f_S' values from Fig. 7. Again, it is clear that for the largest value of f_S' the liquid phase mass transfer can make a significant contribution to the overall coefficient, although the contribution diminishes with increasing $-f_S'q_S$. The smallest value of f_S', on the other, would be judged to have an overall coefficient that is unaffected by the individual liquid phase coefficient over the entire range of $-f_S'q_S$. Thus, at the smaller values of f_S' one may expect a less pronounced peak or even the absence of the peak. However, this does not take account of the effects of finite channel width. In particular, the gas phase Coriolis convection is expected to increase the gas phase mass transfer coefficient significantly. In Figs. 8 and 9 therefore, $k_S f_S'$ will be shifted upwards and k_C will make a larger contribution to the overall mass transfer coefficient.

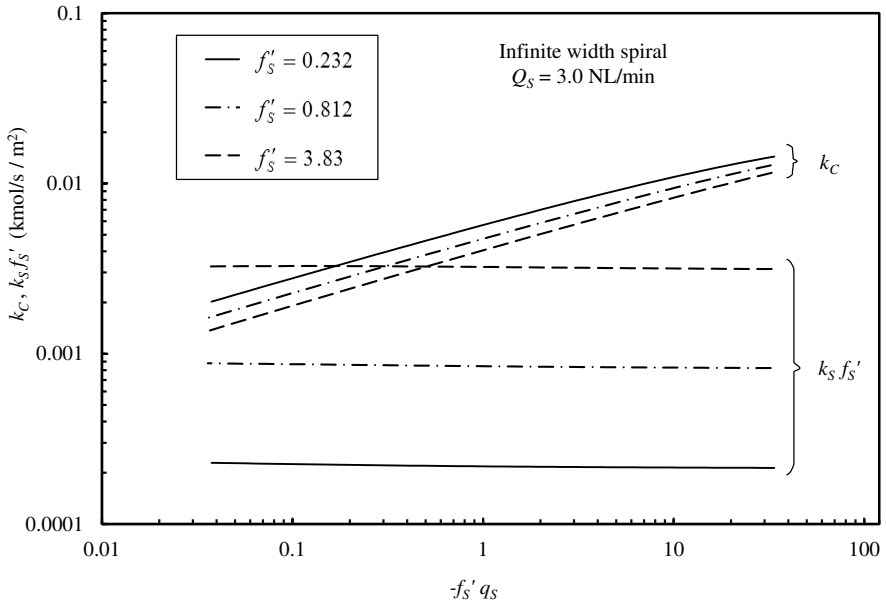

Figure 9. Variation with normalised flow rate ratio of individual mass transfer coefficients for infinite channel width. Plots for the three f_S' values in Fig. 7 with fixed Q_S = 3.0 NL/min.

Direct support is available for the idea that a particular value of liquid layer thickness is associated with the peak in mass transfer coefficient. If that is the case then a plot of $K_C a_P$ should cause the peaks to align for all values of f_S' and Q_S represented in the data.

Such a plot is possible using the liquid layer thickness measurements of MacInnes and Zambri (2015) for the same channel and at the same rotation rate as in the experiments here. The layer thickness is that at the minimum point in the layer, referred to as h_L. The layer thickness data for a wide range of liquid viscosity were shown to collapse well as a function of $\mu_L Q_L$, where subscript 'L' designates liquid phase quantities. Essentially, the driving centrifugal body force dominates the liquid flow and, for a fixed liquid layer thickness, an increasing viscosity requires a decreasing liquid flow rate in order for viscous shear stress at the channel walls to balance body force on the liquid. Appendix A presents a function $h_L(\mu_L Q_L)$ that fits the layer thickness data.

This function allows the liquid layer thickness associated with each data point to be determined using the measured flow rate for that point and the appropriate viscosity value from Table 1. In place of $K_C a_P$, $K_C a_P / f_S'$ is used to remove approximately the dependence on f_S'. Fig. 10 shows the resulting dependence of overall mass transfer coefficient on liquid layer thickness for data at all seven values of f_S' and the three different values of solvent (gas) flow rate, indicated in terms of the corresponding values of solvent Reynolds number, $\mathrm{Re}_S = \rho_S Q_S / w\mu_S$ (as defined in MacInnes et al., 2012, with w the 4 mm channel width). Strikingly, the data generally align quite well, with a peak falling at a liquid layer thickness of around 80 to 90 μm, for this channel, these phase and solute properties and the rotation rate (3200 rpm) of these results. The points at large h_L that lie well above the clustered data correspond curiously to data at the lower temperatures (points for $f_S' = 0.232$, 0.812 and 1.15). The higher surface tension at lower temperature would result in a greater meniscus height and perhaps the liquid layer thickness corresponding to the peak position is corresponding increased. Further shifts are evident as a consequence of solvent Reynolds number, which changes the strength of the Coriolis convection in the solvent phase and consequently the relative importance of the liquid phase mass transfer processes that determine the peak.

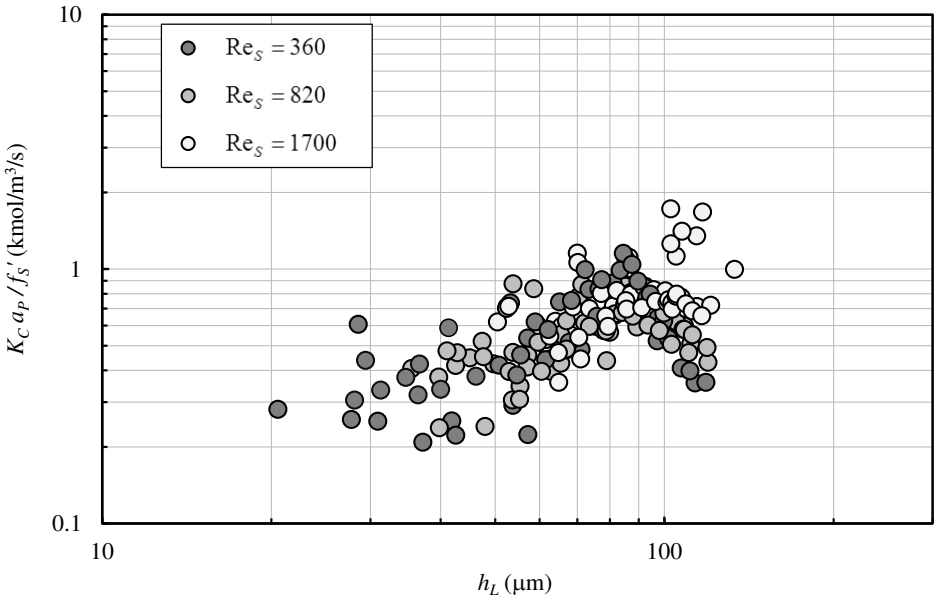

Figure 10. All data for normalised non-dimensional overall volumetric mass transfer coefficient plotted as a function of liquid phase Reynolds number. Symbols are shaded according to gas phase Reynolds number. Data points for $f_S' = 0.232$, 0.812 and 1.15 are shown with grey outlines.

4.2. Relative performance

The previous sections have established the mass transfer characteristics of the experimental spiral operated over a range of solute properties and flow rates. These mass transfer data make it possible now to assess the performance of rotating spiral contacting relative to alternative methods of counter-current contacting. Two alternative methods are considered: the packed column and the rotating packed bed, the former is in widespread use in industry and the latter is a variant using rotation of a packed volume to achieve augmented body force. The packed column data of Houston and Walker (1950) spans a similar range of f_S' in the same phase system as here (water-air) and represents a wide range of both gas and liquid flow rates. Published results for rotating packed beds involve a range of packing types and, again for the water-air system, results spanning a range of f_S' and flow rates are assembled from Liu et al. (1996), Chen and Liu (2002), Lin et al. (2004), Lin and Chien (2008), Chiang et al. (2009) and Hsu and Lin (2012). These references are summarised in Table 2 where the parameters needed to convert the reported mass transfer coefficient values to specific throughput values using the relations in Section 2 are listed.

Table 2. Conditions for the packed column and rotating packed bed data used in the performance comparison. (f' is the equilibrium ratio of gas phase and liquid phase solute mole fractions.)

Reference	Solute (f')	T	Packing	ε	Mode
Packed column data					
Houston & Walker (1950)	ethanol (0.322) methanol (0.282) ammonia (1.08) acetone (2.52)	27 °C	Raschig rings	0.72	absorption
Rotating packed bed data					
Liu et al. (1996)	ethanol (0.220)	20 °C	rectangular solids	0.53	desorption
Chen & Liu (2002)	isopropyl alcohol (0.612) acetone (2.37) ethyl acetate (7.47)	25 °C	beads	0.40	absorption
Lin et al. (2004)	isopropyl alcohol (0.612) ethyl acetate (7.47)	25 °C	wire mesh	0.96	absorption
Lin & Chien (2008)	ethanol (0.290) acetone (2.37) ethyl acetate (7.47)	25 °C	wire mesh blades	0.99	absorption
Chiang et al. (2009)	ethanol (0.389)	30 °C	wire mesh	0.94	absorption
Hsu & Lin (2012)	methanol (0.275) 1-butanol (0.663)	25 °C	wire mesh blades	0.99	absorption

Most of these studies are for absorption and the formulas in Section 2 used in the present desorption experiments continue to apply, although the cleaned phase is now air and the solvent phase water, so f_S' and q_S become ratios of liquid to gas values rather than gas to liquid as for desorption; overall mass transfer coefficient and specific throughput are in terms of gas phase quantities not liquid phase ones. Direct comparison of results for absorption and desorption involving different solutes and operating conditions requires some care. For desorption, the increasing specific throughput with increasing f_S', associated with the decreasing gas flow rate required, can be adjusted approximately by dividing specific throughput by f_S' (as was done with mass transfer coefficient in Fig. 10). In the case of absorption, where the cleaned phase is the gas, no adjustment is needed since the increasing

liquid flow with decreasing f_S' needed to remove the solute does not greatly affect passage volume since the liquid always occupies a minor fraction of the passage.

A further adjustment to specific throughput is needed to allow direct comparison of absorption and desorption results. The gas and the liquid phases have very different densities and so the volume flow rate used in the specific throughput will be inherently larger for absorption since the cleaned phase is the gas. This difference is easily removed by using mole flow rates rather than volume flow rates. So the final normalised total specific throughputs allowing comparisons across different devices, conditions and mass transfer modes are $n_C\Phi_{CN}$ (absorption) and $n_C\Phi_{CN}/f_S'$ (desorption). In the comparisons, 90% removal of the solute ($c_C = 0.1$) is used to fix the number of equilibrium stages, on which total specific throughput depends. Fig. 2 shows that the results will not be greatly changed were other purification values considered.

Fig. 11 shows total specific throughput (Eq. 17), modified as just described, plotted against normalised flow rate ratio for all of the rotating spiral data from the present study and the packed column and rotating packed bed data from the references in Table 2. The spiral data are the dark circles and are approximately collapsed by the modified total specific throughput, a consequence probably of relative insensitivity of mass transfer in the spiral to convective effects. For data violating Eq. 10, it is impossible to achieve the required level of purity ($c_C = 0.1$) and so data for which $-f_S'q_S$ is less than $1-c_C = 0.9$ cannot be plotted. Indeed as the spiral data approach this limit value they decrease rapidly towards zero specific throughput as a consequence of an increasingly large number of stages required to reach $c_C = 0.1$ (Fig. 2).

The packed column data are shown as grey diamonds and, unlike those of the rotating spiral, spread widely both horizontally and vertically. The horizontal spread, extending to normalised flow rate ratio values exceeding 100, simply indicates that data were taken for flow rate ratios corresponding to highly wasteful solute use, those for say $-f_S'q_S > 10$. The scatter in the vertical direction is principally associated with the gas flow rate used, the larger the gas flow rate the greater the specific throughput, with the topmost data nearing the theoretical flooding limit (Sherwood et al., 1938). This sensitivity to gas flow rate is typical in reported data for packed columns (e.g. Onda et al., 1968) and highlights an inherent weakness of contacting schemes that allow the phases to mix: a large relative velocity between the phases is crucial for producing the small droplet (or bubble) sizes and the strong

convective motions needed to promote effective mass transfer, but this relative velocity is restricted by the equilibrium constraint on the ratio of phase flow rates, flooding and the requirements of good liquid distribution over the packing. From Fig. 11, the present rotating spiral channel gives several times greater total specific throughput than the packed column in the vicinity of the expected flow optimum, i.e. around $-f_S' q_S = 4$.

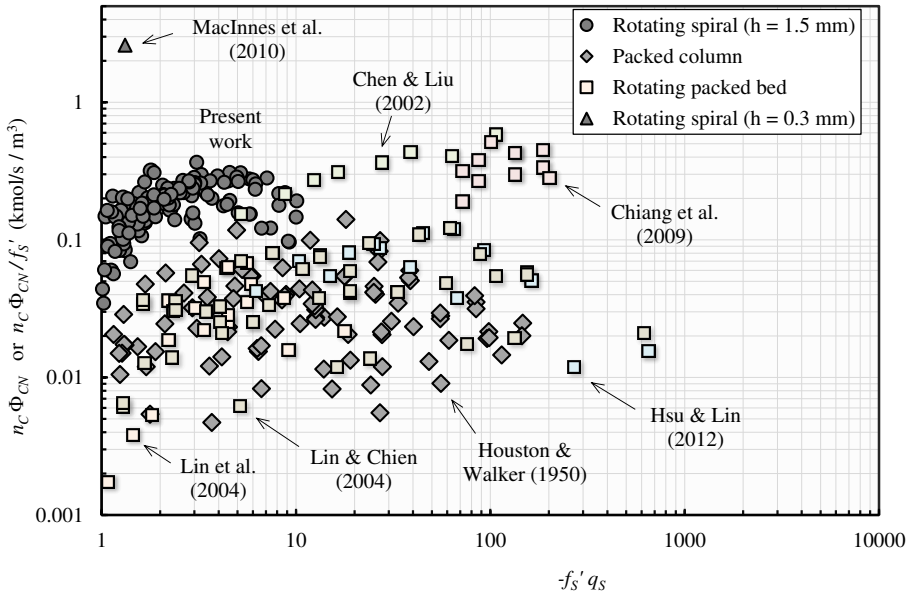

Figure 11. Normalised total specific throughput computed from the experimental data taken over a range of phase and solute systems and phase flow rates for the rotating spiral, packed column and rotating packed beds.

Over the top of the other data are lightly-shaded squares representing the data for rotating packed beds. A similar proportion of the data as for the packed column are at $-f_S' q_S > 10$, hence using excessive solvent flow rate. Interestingly, for some of the studies in this range of large $-f_S' q_S$ (Chiang et al., 2009 and Chen and Liu, 2002) the total specific throughput greatly exceeds that of the packed bed, but as flow rate ratio drops below $-f_S' q_S = 10$ the rotating packed bed performance is similar to that of the static packed column. Only one study shows a specific throughput below $-f_S' q_S = 10$ that is comparable with those for the current rotating spiral. Two points of Chen and Liu (2002) fall in this range and achieve a specific throughput just 40% lower than for the rotating spiral.

Since all of the packed bed data (whether for a rotating or a static bed) shown on the plot are for absorption, the gas phase is the cleaned phase in each case and the excessive

normalised flow rate ratios therefore correspond to gas flow rates that are far too small in relation to the liquid flow rates being used. This becomes a problem when separation is attempted for a solute that favours the liquid phase at equilibrium, say ethanol in the water-air system. Then, for either absorption or desorption of the solute, the gas flow rate must be relatively large. In the case of absorption, failing to achieve that large gas flow simply means excessive use of solvent as is the case for the results of Chiang et al. (2009) for absorption of ethanol with a rotating packed bed. But for desorption, a too small gas flow rate means $-f_S' q_S$ falls below the critical value and separation is not possible, as happens for the results of Liu et al. (1996) for desorption of ethanol from water. The data are taken at around $-f_S' q_S = 0.004$ for which the best possible purification that can be achieved is, from Eq. 11, 0.996, i.e. only 0.4% of the incoming solute can be removed. This is nearly identical to the purification achieved for co-current flow at the same flow rate ratio (Eq. 20 for $\zeta \to \infty$).

Finally, it is important to note that the size of the spiral channel can be decreased to increase specific throughput. As mentioned, specific throughput increases inversely with the square of channel height. To compensate for the increase in relative surface tension force at smaller scale, one can simply increase the rotation rate. The stripping distillation of a binary mixture reported in MacInnes et al. (2010) is for an experimental spiral channel of height 0.3 mm rotating at 5000 rpm. The purification achieved was well captured using individual mass transfer coefficients determined by 2D numerical computations (Ortiz-Osorio et al., 2009) over the range of possible bulk mole fraction. Using the computed mass transfer coefficient values at dilute concentrations of the most volatile species allows a calculation, just as for the other data here, of desorption of the most volatile species from a mixture with the other majority species into a gas stream of that majority species. This calculation results in the triangle shown on Fig. 11 which is very near to the factor of 25 increase in specific throughput that is expected relative to the present 1.5 mm spiral channel. Thus, reduction in channel size and the resulting reduction in both device size and contacting time scale appears to be a straightforward direction of improvement for the rotating spiral.

5. Discussion and Conclusions

Measurements of desorption of organic solutes from water into air using a rotating spiral channel have been presented for a range of water flow rates, air flow rates and solute equilibrium characteristics (the slope of the solute equilibrium curve, f_S'). These are used to

quantify the mass transfer performance of this type of device for the first time. It is argued based on bulk flow relations for continuous contacting that two important parameters drive the effectiveness of the mass transfer. The first is the ratio of the phase flow rates, which determines sufficiency of solvent flow, and the second is the specific throughput, which is a measure of contacting effectiveness and emerges naturally from bulk relations for purification.

Results are probed using the analytical solution for an infinitely wide spiral channel and it is found that this approximation to the finite width experimental channel captures the major trends. Significant quantitative differences are observed, however, and these are interpreted in terms of the changing central liquid layer thickness in relation to the greater thickness under the menisci formed at the end walls of the channel. As the liquid flow rate decreases, the liquid layer thickness decreases and an increasing proportion of liquid flow is shifted from the main central layer to the corner regions under the menisci. At first the liquid mass transfer is dominated by the good mass transfer in the thin central layer and the mass transfer coefficient rises with decreasing liquid flow rate. Eventually, with further decrease in liquid flow rate the increasing proportion of flow in the corner regions, where mass transfer is poor, leads to a decreasing mass transfer coefficient, resulting in a peak in mass transfer coefficient. This behaviour is dependent on the liquid phase making a significant contribution to the overall mass transfer coefficient and the infinite channel width model, which resolves the individual mass transfer coefficients, is used to show that the individual liquid mass transfer coefficient can be expected to contribute significantly but to an extent that varies with f_S' and gas flow rate.

Using previous liquid layer thickness measurements in the same experimental spiral (MacInnes and Zambri, 2015), the peak in mass transfer coefficient was shown to occur at roughly the same layer thickness, and hence liquid flow rate, independent of solute equilibrium characteristics or gas phase flow rate. This independence allows selection of gas flow rate to produce the optimum phase flow rate ratio (for any particular solute characteristic) at the same time that the mass transfer coefficient is optimum. For other channel aspect ratios, meniscus heights and liquid viscosities than in these experiments, it is likely that the peak in specific throughput would continue to be found, although at perhaps somewhat different liquid layer thickness. It is interesting to note that it is also likely that the peak position can always be adjusted to occur at the optimum phase flow rate ratio, thus simultaneously optimising for device size and solvent cost.

The rotating spiral is currently an emerging contacting approach and it is important that these new results are placed into the context of existing alternative methods. For this purpose, a modified total specific throughput is used to allow meaningful comparison of results taken from different devices and whether absorption or desorption is involved. This total specific throughput is related inversely to device size and processing time scale. Comparisons with packed column and rotating packed bed data from the literature shows that the present rotating spiral allows device size to be many times smaller than for these alternative methods. Further, the dependence of device volume on the square of channel size is demonstrated using previous distillation data from a rotating spiral with a smaller channel size than that used here.

While the wide-channel model of MacInnes et al. (2012) for rotating spiral contacting has captured the main trends of the data, significant differences caused by the finite width of the experimental channel have been found. This makes it attractive to include an account of the actual finite width channel section in future computations where precise prediction is needed.

Acknowledgements

We thank the Iraqi Government for an HCED Scholarship (D 11-3508) supporting AAA.

Appendix A

Data for liquid layer thickness, given in Fig. 13 of MacInnes and Zambri (2015), can be used to develop a correlation for liquid layer thickness (the minimum thickness in the layer), h_L, in terms of the product of liquid viscosity and liquid volume flow rate, $\mu_L Q_L$. The data are for the same channel and rotation rate used in the present experiments, so the resulting correlation applies here. While the thickness data are for a gas flow rate of 1.15 NL/min, i.e. lower than those used here, the same reference demonstrates the relatively minor effect that gas flow rate has on liquid layer thickness at 3200 rpm.

Fig. A1 shows a plot of the data (symbols) and the collapse with independent parameter $\mu_L Q_L$ for a range of data spanning two orders of magnitude of liquid viscosity. A reasonable fit is given by the function shown as a solid curve, which is given by

$$h_L = (\mu_L Q_L)^{1/3}\left[6.2\times10^{-4} - 5.3\times10^{-8}(\mu_L Q_L)^{-1.06}\right] \qquad \text{(A1)}$$

The dashed line is the result for the infinitely wide channel, in the case of water viscosity. Keeping only the constant term in square brackets in Eq. A1 produces this result, giving liquid layer thickness proportional to $(\mu_L Q_L)^{1/3}$. The finite width channel gives an increasingly thinner layer relative to a wide channel as the liquid layer thins, since an increasing proportion of the liquid flow is diverted to the corner regions under the menisci.

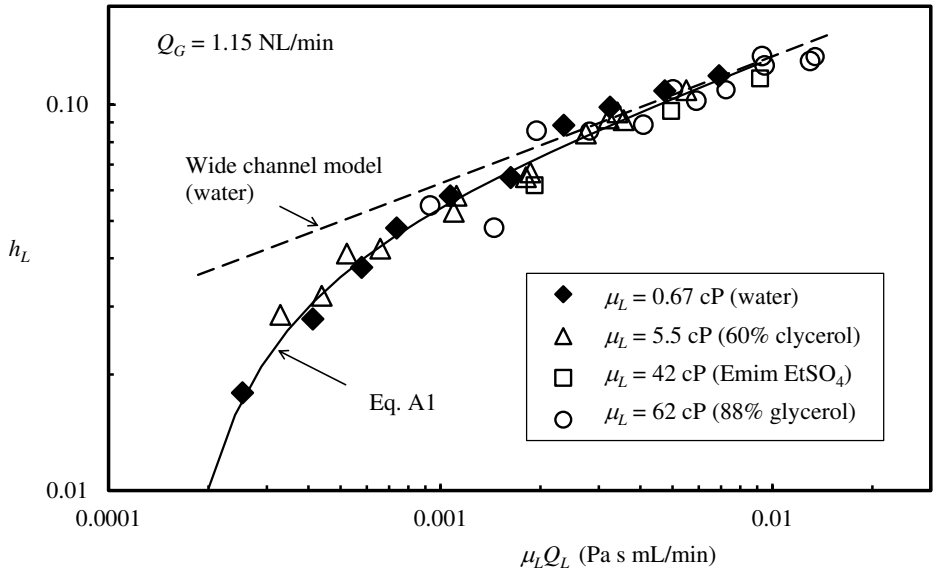

Figure A1. Correlation for liquid layer thickness as a function of $\mu_L Q_L$ for the experimental channel and 3200 rpm rotation rate. Data from MacInnes and Zambri (2015).

References

Anderson, T. F. and J. M. Prausnitz, 1978, Application of the UNIQUAC Equation to Calculation of Multicomponent Phase Equilibria. 1. Vapor-Liquid Equilibria, Ind. Eng. Chem. Process Des. Dev., 17 (4), 552-561.

Chen, Y.-S. and H.-S. Liu, 2002, Absorption of VOCs in a Rotating Packed Bed, Ind. Eng. Chem. Res., 41 (6), 1583-1588.

Chiang, C.-Y., Y.S. Chen, M.S. Liang and F.-Y. Lin, C. Y.-D. Tai, H.-S. Liu, 2009, Absorption of ethanol into water and glycerol/water solution in a rotating packed bed, J. Taiwan Institute of Chemical Engineers, 40, 418-423.

Edmister, W. C., 1957, Absorption and Stripping-factor Functions for Distillation Calculation by Manual and Digital-computer Methods, A.I.Ch.E. Journal, 3 (2), 165-171.

Fuller, E. N., K. Ensley and J. C. Giddings, 1969, Diffusion of Halogenated Hydrocarbons in Helium. The effect of Structure on Collision Cross Sections, The Journal of Physical Chemistry, 73 (11), 3679-3685.

Hayduk, W. and H. Laudie, 1974, Prediction of Diffusion Coefficients for Nonelectrolytes in Dilute Aqueous Solutions, A.I.Ch.E. J., 20 (3), 611-615.

Houston, R. W. and C. A. Walker, 1950, Absorption in Packed Towers Effect of Molecular Diffusivity and Gas Film Coefficient, Industrial and Engineering Chemistry, 42 (6),1105-1112.

Hsu, L.-J. and C.-C. Lin, 2012, Binary VOCs absorption in a rotating packed bed with blade packings, J. Environmental Management, 98, 175-182.

Khattab, I. S., F. Bandarkar, M. A. A. Fakhree and A. Jouyban, 2012, Density, viscosity and surface tension of water+ethanol mixtures from 293 to 323 K, Korean J. Chem. Eng., 29 (6), 812-817.

Liu, H.-S., C.-C. Lin, S.-C. Wu and H.-W. Hsu, 1996, Characteristics of a Rotating Packed Bed, Ind. Eng. Chem. Res., 35, 3590-3596.

Lin, C.-C., T.-Y. Wei, W.-T. Liu and K.-P. Shen, 2004, Removal of VOCs from Gaseous Streams in a High-Voidage Rotating Packed Bed, J. Chemical Engineering Japan, 37 (12) 1471-1477.

Lin, C.-C. and K.-S. Chien, 2008, Mass-transfer performance of rotating packed beds equipped with blade packings in VOCs absorption into water, Separation and Purification Technology, 63, 138-144.

MacInnes, J. M., Ortiz-Osorio, J., Jordan, P. J., Priestman, G. H. and Allen, R. W. K., 2010, Experimental Demonstration of Rotating Spiral Microchannel Distillation, Chemical Engineering Journal, 159 (1-3), 159-169.

MacInnes, J. M., M. J. Pitt, G. H. Priestman and R. W. K. Allen, 2012, Analysis of two-phase contacting in a rotating spiral channel. Chemical Engineering Science, 69, 304-315.

MacInnes, J. M. and M. K. S. Zambri, 2015, Hydrodynamic Characteristics of a Rotating Spiral Fluid-phase Contactor, Chem. Eng. Sci., 126, 427-439.

MacInnes, J. M., A. A. Ayash and G. R. M. Dowson, 2017, CO_2 absorption using diethanolamine-water solutions in a rotating spiral contactor, Chemical Engineering Journal, 307, 1084-1091.

Onda, K., H. Takeuchi and Y. Okumoto, 1968, Mass Transfer Coefficients Between Gas and Liquid Phases in Packed Columns, J. Chemical Engineering Japan, 1 (1), 56-62.

Ortiz-Osorio, J., J. M. MacInnes, P. J. Jordan, G. H. Priestman and R. W. K. Allen, Computation of Mass Transfer for Rotating Spiral Microchannel Distillation, 8th World Congress of Chemical Engineering, Montreal, July 2009.

Podbielniak, W. J., 1935, Centrifugal Fractionation Method and Apparatus, U. S. Patent 2,003,308.

Podbielniak, W. J., 1936, Method of Securing Counter Current Contact of Fluids by Centrifugal Action, U. S. Patent 2,044,996.

Podbielniak, W. J., 1937, Method and Apparatus of Refining Hydrocarbon Oil, U. S. Patent 2,093,645.

Podbielniak, W. J., 1938, Apparatus for Effecting Counter Current Contact Between Fluids, U. S. Patent 2,109,375.

Podbielniak, W. J., H. R. Kaiser and G. J. Ziegenhorn, 1970, Centrifugal Solvent Extraction, in The History of Penicillin Production, A. L. Elder, Editor, Chem. Eng. Prog. Symp. Series, No. 100, 46, New York: American Institute of Chemical Engineers.

Saleh, M. A., S. Akhtar and M. S. Ahmed, 2006, Density, viscosity and thermodynamic activation of viscous flow of water+acetonitrile, Physics and Chemistry of Liquids, 44 (5), 551-262.

Sherwood, T. K., R. L. Pigford and C. R. Wilke, 1975, Mass Transfer, McGraw-Hill.

Sherwood, T. K., G. H. Shipley and F. A. Holloway, 1938, Flooding velocities in packed columns, Ind. Eng. Chem., 30, 765-769.

Thomas, K. T. and R. A. McAllister, 1957, Densities of Liquid-acetone-water Solutions up to Their Normal Boiling Points, A.I.Ch.E. J., 3 (2), 161-164.

Wilke, C. R. and P. Chang, 1955, Correlation of diffusion coefficients in dilute solutions, A.I.Ch.E. J., 1 (2), 264-270.